2023 IEEE International Conference on Robotics and Automation (ICRA 2023)
May 29 - June 2, 2023. London, UK

Disturbance Observer Based Contact Detection for Motorized Hydraulic Actuators

Chunpeng Wang[1] and John P. Whitney[1,2]

Abstract— **Contact detection without endpoint tactile sensing is challenging; friction and inertia obscure the sensing of low amplitude and high frequency forces. In this work we explore fluidic transmissions as series-elastic actuators, coupled to remotely-located direct-drive brushless motors, in a bid to maximize low-impedance sensitivity to contact while maintaining high bandwidth. We employ a disturbance observer to remove motor friction and further reduce minimum impedance. Using a 2-DOF remotely-actuated hydraulically-coupled robotic gripper, we demonstrate a maximum endpoint Z-width of 40dB and a robust contact detection threshold of 0.2N, without endpoint tactile sensing or joint position sensing. These results enable wiring-free and joint sensor-free arm and end-effector design, which are of particular interest for human-robot interaction, harsh-environment, magnetically-sensitive, and low-cost robotic manipulators that must maintain high bandwidth and high contact sensitivity.**

I. INTRODUCTION

Detecting a contact only by force sensing is an attractive robotic manipulation research. An accurate and sensitive contact force can improve manipulation speed and help avoid damaging fragile object in a telerobotic system with force feedback [1], [2]. One requirement for safe contact and sensitive force sensing is soft interaction with environment [3], which is important in physical human-robot interaction while a stiff manipulator is still highly desirable when high bandwidth performance is needed. Haptic interfaces, in particular, seek to maximize the ratio between maximum and minimum endpoint impedance ("Z-width") [4], giving the ability to render the widest possible range of virtual environments[3]. Two classic, complementary approaches to this challenge are the use of high-performance mechanical transmissions to offload the actuator mass from the moving mass of the manipulator to the base, as exemplified by the Whole Arm Manipulator [5], and high-bandwidth endpoint force-feedback (e.g. admittance control) which is designed to render a specific desired endpoint admittance and actively compensate for sources of mechanical friction. A long-recognized limitation is that force-feedback cannot significantly reduce the physical endpoint inertia without jeopardizing the closed-loop system stability [6], [7], [8]. However, this restriction can be circumvented if purposeful physical compliance (so-called "series elasticity") is added between the actuator and the endpoint [9], [10].

Fluid-powered actuators, and soft fluid actuators in particular [11], have inherently high force density [12], allowing for low endpoint mass even for serial-chain manipulators with many degrees of freedom. By adjusting the volumetric compliance and internal geometry of the transmission hoses, a purposeful series elasticity and damping can be tuned [13]. The measurement of the internal pressure in the hydraulic or pneumatic line affords an estimate of the joint torques. However, any static friction at the endpoint (e.g. hydraulic seal friction) will not be observable from internal pressure measurements.

Contact detection without any endpoint force sensing is the next challenge. Momentum observer in [14] is used for rigid robot links, and the augmented version [15] can also be applied to SEA system [9] where there's compliance between motor and joint, but require known series stiffness. Soft-continuum and diaphragm-type fluid actuators based on material elasticity and/or non-rubbing diaphragm seals exhibit nearly-zero static friction, allowing external interaction forces to be estimated with high precision using only internal fluid pressure measurements. This is similar to the augmented version of momentum observer with flexible joint, but the transmission model is more complex due to equivalent fluid inertia [16].

In this paper we investigate to maximize impedance range of fluid-actuated systems and make contact decision based estimated external force with internal force. Section II describes three classical haptic interface and the exemplary system, a 2-DOF lightweight gripper with details on fluid pressure force feedback setup. Section III describes the disturbance observer (DOB) force feedback method, adapted to the case of fluid-actuated systems, and presents detailed Z-width measurements. Section IV describes a model-based approach to estimate external force and a contact detection for the fluid-actuated system. The accompanying video shows operation of the gripper, passive behavior, the qualitative minimum and maximum impedance performance, and contact detection for rigid and soft objects.

II. HAPTIC SYSTEM

Maximizing the dynamic range of a manipulator's endpoint impedance requires a collaboration between the physical hardware and closed-loop feedback control design. Fig. 1(A), (B) and (C) show three common motorized

*This work is supported in part by NSF NRI 1830425 and the U. S. Office of Naval Research under award number N00014-19-1-2131

[1]The authors are with the department of Mechanical and Industrial Engineering, Northeastern University, Boston, MA 02115, USA.

[2]corresponding author, j.whitney@northeastern.edu

[3]In this paper, we use the term "impedance" in both the formal sense (mechanical impedance for linear systems is defined as $Z(s) = F(s)/V(s)$, where s is the Laplace variable and F and V are the port force and velocity respectively) and the informal sense, referring simultaneously and variably to stiffness, friction, mass, and damping. In informal usage, "low impedance" usually refers to minimizing the stiffness and friction which dominate low-frequency characteristics of a mechanical system.

haptic interface, where the primary sensory feedback signals are shown with solid lines, and less-commonly employed feedback signals are shown dashed. V_e and V are the external (endpoint) and driving-point (motor) velocities, F_p is the transmission internal force, and F_e is the external (endpoint) force. Fig. 1(D) shows the model of traditional SEA system, where F_a is the applied motor force, F_f is motor friction, m is motor inertia, and k_s is the series stiffness[4].

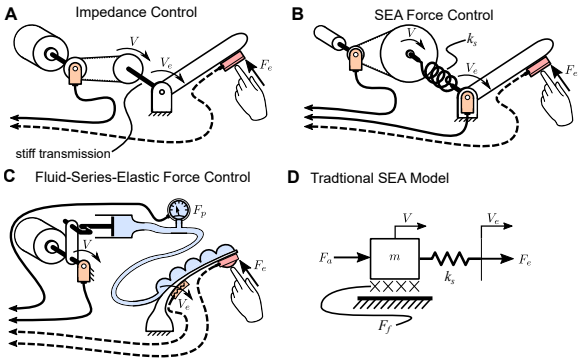

Fig. 1: Force feedback systems, with primary feedback signals (solid) and secondary feedback signals (dashed). **(A)** Stiff transmission configuration, with stiff coupling between motor and endpoint link. **(B)** Series-elastic configuration, where purposeful compliance allows an estimate of internal force using dual encoder feedback. **(C)** Series-elastic system with series fluid connection between motor and endpoint link. **(D)** 2-DOF series-elastic system model with force and parameter definitions.

A. Actuation and Control Architecture

In the impedance control approach [17], [18], a low-friction actuator drives a joint via a stiff series connection Fig. 1(A); driving-point state feedback is used to render the desired endpoint impedance, and the stiff transmission ensures that the driving-point impedance is reflected at the endpoint accurately. However, without force feedback, the system cannot render an endpoint impedance below the passive impedance (i.e. friction and inertia) of the motor/gearbox/actuator. In the *series elastic actuation (SEA)* approach, as shown in Fig. 1(B), the transmission stiffness is purposefully reduced, easing the requirements on closed-loop bandwidth; as the driving-point and endpoint become increasingly decoupled, it is easier to stably compensate for actuator-side friction and mass [9], [19], [20]. Achieving maximum performance may entail external force sensing in addition to full-state feedback, but more commonly, the external force is estimated via the internal force F_p in the transmission elastic element as $F_p = \int k(V_e - V)dt$.

[4]Note: In this paper, our equations and models use the translational lumped-element equivalent system convention, while the experimental system employed is a rotational system. References to forces and velocities are given/plotted in the corresponding rotational (torque/angular velocity) units, and presented in the motor frame unless otherwise noted. Internal fluid pressure is converted to the equivalent internal force, F_p, which for the experimental system is reported as an internal torque acting on the motor, in units of Newton-meters.

Mechanical-spring SEA designs require the actuator and external joint to be located in close proximity, resulting in high endpoint mass for proximal degrees of freedom in serial-chain manipulators. Fluid-actuated systems (Fig. 1(C)) offer a variation on the traditional SEA configuration; with a remote actuator and the mechanical spring replaced by a fluid-filled hose and internal force now measured with a pressure sensor. The series compliance and damping are tuned by controlling the volumetric stiffness and internal geometry of the hydraulic line [13], or, in the case of a soft-continuum actuator, modification of the material and geometry of the endpoint actuator. Soft-material strain and force sensors can be added to these systems at the endpoint, giving high-quality endpoint state and force information [11]. This eliminates the need to model the internal stiffness and damping properties of the soft actuator, but presents challenges for high-bandwidth control due to sensor-actuator non-collocation—achieving an equivalent level of performance without any endpoint sensing is highly desirable.

Force feedback control is a simple and direct way to compensate for mechanical impedance [21]. Theoretically, this system can be shown to be passive for any feedback gain $K_f \geq -1$, where "passive" refers to a system that is stable when in contact with any potential environmental impedance [22]. However, every real system has some internal degrees of freedom, whether purposeful (series elastic actuation) or incidental (internal vibration modes), creating a situation of non-collocation between sensing and actuation ports. Many methods to improve impedance compensation performance beyond simple proportional force-feedback have been proposed, including *force feedback loop shaping*, where a general force feedback filter replaces the proportional force gain, $K_f \rightarrow K_f(s)$ [23], *natural admittance control (NAC)* [24], *model-based force control* [25], and the *disturbance observer (DOB)* control method [26]. These equivalent methods, rather than applying force feedback control effort uniformly across all frequencies, allow high-gain force feedback to target only the lower frequencies where friction, stiffness, and damping of the system dominate, without attempting to reduce inertia at higher frequencies, beyond causality and passivity limits.

B. Fluid-actuated Testbed Setup

A low impedance hardware requires minimum motor inertia and friction, also small gear ratio or no gear box. Our testbed, a motorized fluid-actuated system with a rolling-diaphragm-actuated 2-DOF gripper [27], is shown in Fig. 2. Each actuator is a double-acting piston sealed by low friction fiber-elastomer rolling-diaphragms. The two diaphragm actuators drive independent fingers, affording wrist pitch and gripper pinch DOFs; the input ends of the transmission are connected to individual direct-drive brushless motors (Akribis ACD120-80) via fiber-reinforced rubber hoses, and the motor is coupled via rotary versions of the diaphragm actuators, introduced in [28]. This approach combines the low mass and friction of soft fluid actuators with the controllability and performance of direct-drive SEA. Fluid

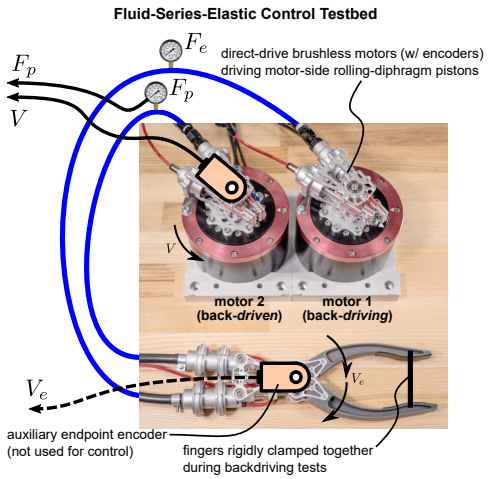

Fig. 2: Diaphragm-actuated 2-DOF gripper. Testing endpoint impedance by using one finger to backdrive the other with a torque chirp signal on back-driving motor (two fingers band together using electrical tape). Testing multi-DOF lumped mass-spring model for hose, water and end-effector finger by using back-driven motor and finger only with a torque chirp signal on backdriven motor (fingers are separate). External force F_e and internal force F_p are measured based on hose pressure, cylinder pressure area and actuator geometry.

pressure is recorded using an analog input EtherCAT terminal with 16bit resolution. A temporary optical encoder made by US DIGITAL with maximum resolution 10,000 pulses/rev (40,000 counts/rev with quadrature) is used to measure the position of the backdriven joint finger during system identification (not used for control). The low-level control code uses the Simple Open EtherCAT Master (SOEM) library with the main control loop running at 2kHz on an isolated CPU core. More details of testbed setup can be found in [27].

III. MOTOR FORCE FEEDBACK CONTROL

The maximum endpoint impedance of our fluid-actuated system is a series stiffness of motor impedance (K_p gain of PD controller) and hose stiffness. It can be achieved by choosing a stiffer hose and set maximum K_p gain. The minimum endpoint impedance is coming from diaphragm stiffness at gripper side when motor impedance is set to zero. The following work shows an approach to minimize motor impedance by disturbance observer.

A. Disturbance Observer Framework

Disturbance observers use state measurements and a nominal inverse model of the system plant to estimate the expected external force; this is compared to the actual external force, with the difference becoming an estimate of the disturbance, which is then subtracted from the motor input command to remove the disturbance. For a fluid actuated manipulator, we use the equivalent internal force F_p from transmission fluid pressure. The sum of forces on the motor is

$$F_a(s) + F_p(s) - F_f(s) = P^{-1}(s)V(s), \tag{1}$$

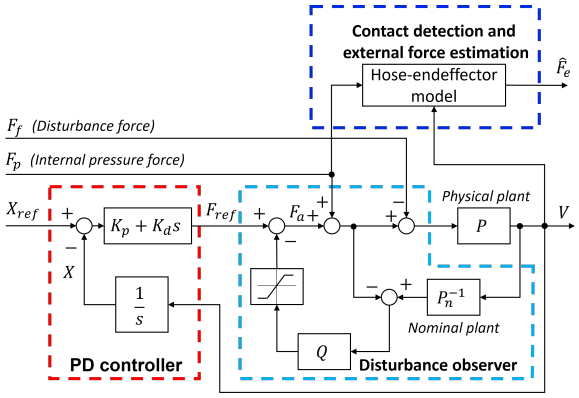

Fig. 3: Disturbance observer for 1-DOF actuator motor plant with PD controller and hose-endeffector model for contact detection and external force estimation. The disturbance is estimated by comparing force input and velocity output times a nominal plant.

where the linear approximated motor plant $P = (ms + b + k/s)^{-1}$. From the controller block diagram,

$$\begin{aligned} F_a(s) =& \frac{1}{1-Q(s)} F_{ref}(s) + \frac{Q(s)}{1-Q(s)} F_p(s) \\ & - \frac{Q(s)}{1-Q(s)} P_n^{-1}(s) V(s), \end{aligned} \tag{2}$$

where F_{ref} is the reference force (e.g. set by an outer-loop position controller), P_n is the nominal plant, and Q is a low-pass filter. The order of Q depends on the order of motor plant. Since the inverse of nominal plant is $P_n^{-1} = m_n s + b_n + k_n/s$, Q must be at least first order to make QP_n^{-1} a proper transfer function [29]. Thus, we choose $Q(s) = \lambda/(s+\lambda)$, where λ is the cut-off frequency of low-pass filter. Since human input frequency is from $4Hz$ to $8Hz$ [30], we can set cutoff frequency to $20Hz$ for the low-pass filter to limit the uncertainty or noise of system and maintain low frequency interaction at the same time. In low frequency limit ($\omega < \lambda$), $Q \approx 1$. Combining Eqs. 1–2 and assuming for low frequency range, the expression for velocity can be written as

$$V(s) = P_n(s) \left(F_{ref}(s) + F_p(s) \right), \tag{3}$$

and so, the closed-loop system dynamics approach the nominal plant. By selecting a frictionless nominal plant $P_n = 1/m_n s$, rather than the best linear approximation of the actual plant, the DOB can theoretically compensate for all internal friction without modifying the system inertia.

To render minimum endpoint impedance, our reference/target force is $F_{ref} = 0$; then Eq. 2 simplifies to

$$F_a(s) = \frac{\lambda}{s} (F_p(s) - P_n^{-1}(s) V(s)). \tag{4}$$

We can think of P_n^{-1} as a target impedance, which in the classic force-feedback example, would be set to zero, and the control signal is thus the integral of the difference between the measured force and the force predicted from a target (zero) impedance, $F_a(t) = \lambda \int_0^t F_p(\tau) \mathrm{d}\tau$; integral

force feedback is very commonly used in force-feedback systems [31].

B. Passivity Requirement

The passivity criterion for linear time-invariant 1-port system [32] is a useful tool to check the overall contact or coupled stability with any passive system. We can use it to determine the possible range of parameters of nominal plant P_n. A linear time-invariant 1-port is passive if and only if (i) its port admittance $Y(s)$ has no poles in the right half plane, (ii) imaginary poles of $Y(s)$ are simple with positive real residues, and (iii) $Re\{Y(j\omega)\} \geq 0$. To check passivity criterion of the disturbance observer, we use an equivalent parallel stiffness and damping to represent friction for 1-DOF motor plant. The admittance of system considering DOB is shown as:

$$\begin{aligned} Y(s) = \frac{V(s)}{F_p(s)} &= \frac{1}{(1-Q(s))\,P^{-1}(s) + Q(s)P_n^{-1}(s)} \\ &= \frac{s\,(s+\lambda)}{ms^3 + (\lambda m_n + b)\,s^2 + (k + \lambda b_n)\,s + \lambda k_n}, \end{aligned} \tag{5}$$

where m_n, b_n and k_n are the nominal mass or inertia, nominal damping and nominal stiffness of 1-DOF motor plant. The overall passivity criterion requires:

$$m_n \geq m - b/\lambda \quad \text{and} \quad 0 \leq k_n \leq k + \lambda b_n. \tag{6}$$

Note that the series dynamics and endpoint inertia, damping, and friction may all be considered part of the passive environment coupled to the motor plant, so the passivity result holds for the whole system. Put the boundary result from Eq. 6 into Eq. 5, the admittance turns out to be:

$$Y(s) = \frac{s+\lambda}{ms^2 + \lambda m s} \tag{7}$$

Below cutoff frequency λ, we have equivalent zero damping and zero stiffness, and the physical inertia is maintained. Above cutoff frequency λ but below active force bandwidth, we have zero stiffness and damping equals to λm, the equivalent inertia is still the physical inertia. From this result, we can see the lower bound of 1-DOF system impedance using DOB force control is the physical inertia, same result shown in [24], [25]. A larger cutoff frequency λ is desired to expand low frequency range for minimum impedance, with the cost to set a larger integral gain potentially destabilizing system.

C. Controller Performance

After applying DOB, the internal pressure force (cyan curve), is following/targeting zero (Fig. 4(A)), where almost zero force is needed for driving motor around and external hysteresis loops also shrink. Also notice Fig. 4(B) shows the identified endpoint impedance, with and without force feedback. The DOB controller reduces endpoint impedance $|Z(j\omega))|$ by 7–10dB up to 10rad/s compared to the passive case. Z-width is calculated by comparing force-feedback targeting zero impedance to a stiff PD controller attempting to clamp the backdriven motor (maximum finger stiffness, red line). As shown in Fig. 4(B), the Z-width range that can be rendered is ~ 42 dB up to 3 rad/s and > 30 dB up to 10 rad/s. The dashed red line ("MaxZ Motor Only") is the maximum impedance measured at the motor output port ($F_p(s)/V(s)$), representing the maximum endpoint impedance *if* rigid hoses were used instead of rubber hoses here, which have modest volumetric compliance. In the rigid-hose case, the theoretical maximum Z-width is 60 dB at DC.

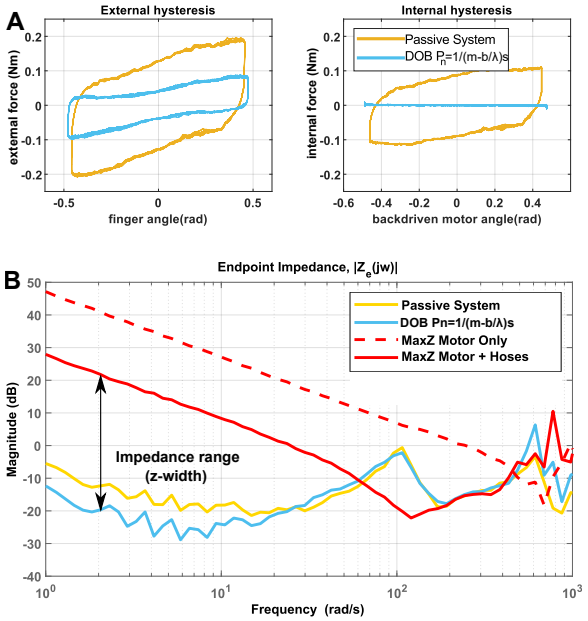

Fig. 4: Experimentally measured gripper performance with force feedback. **(A)** compare the external hysteresis loops F_e/X_e and internal hysteresis loops F_p/X for a quasi-statically backdriven finger ($\omega = 1$ rad/s, amplitude = 0.5 rad). **(B)** Identified endpoint impedance $Z(s) = F_e(s)/V_e(s)$. Z-width comparison is made against the case (red) where the backdriven motor is commanded to hold with maximum stable PD gains.

The supplemental video part (i) shows nominal operation of the gripper with mid-range PD gains; (ii) shows passive backdrivability with motors off (impedance shown as yellow curve in Fig. 4(B), backdriving force shown as yellow curve in Fig. 4(A) external hysteresis); (iii) shows backdriving with force feedback (active zero impedance mode, impedance shown as cyan curve in Fig. 4(B)); (iv) the gripper crushes an empty aluminium beverage can under max PD gains (impedance shown as red curve in Fig. 4B).

IV. FORCE ESTIMATION AND CONTACT DETECTION

Traditional SEA system model Fig. 1(D) uses simple spring model for estimating external force and any load after spring as external input F_e. The simple linear spring model does not fit well in our system since each finger and water inside hose has inertia that cannot be ignored. We will extend the traditional SEA model using a linear lumped model [16] with multiple segments. The number of added

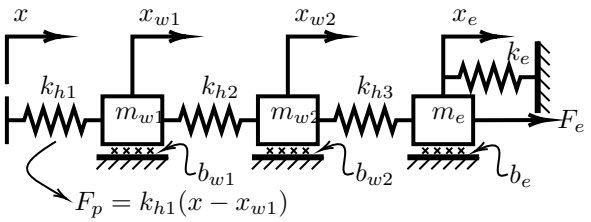

Fig. 5: Three DOF lumped mass-spring model. x, x_{w1}, x_{w2} and x_e are the position of motor, two lumped mass for water in hose, and end-effector finger; m_{w1}, m_{w2} are the two lumped mass for water, and b_{w1}, b_{w2} are the corresponding damping; k_{h1}, k_{h2}, k_{h3} are the separated equivalent spring of hose, and the total spring stiffness would be the equivalent series stiffness; m_e, b_e and k_e are the end-effector's mass, damping and stiffness, and $F_p = k_{h1}(x - x_w1)$ is the model of measured force from pressure reading.

DOF is determined by the real system and frequency range we're interested in.

A. Multi-DOF Lumped Mass-spring Hose Model

In Fig. 5, we demonstrate a 3-DOF lumped mass-spring model for hose and end-effector. Consider x and F_e as input, F_p and x_e as output, and positions and velocities of lumped mass as states, the whole system can be represented as:

$$
\begin{aligned}
X &= \begin{bmatrix} x_{w1} & x_{w2} & x_e & \dot{x}_{w1} & \dot{x}_{w2} & \dot{x}_e \end{bmatrix}, \\
\dot{X} &= \begin{bmatrix} 0 & 0 & 0 & 1 & 0 & 0 \\ 0 & 0 & 0 & 0 & 1 & 0 \\ 0 & 0 & 0 & 0 & 0 & 1 \\ -\frac{k_{h1}+k_{h2}}{m_{w1}} & \frac{k_{h2}}{m_{w1}} & 0 & -\frac{b_{w1}}{m_{w1}} & 0 & 0 \\ \frac{k_{h2}}{m_{w2}} & -\frac{k_{h2}+k_{h3}}{m_{w2}} & \frac{k_{h3}}{m_{w2}} & 0 & -\frac{b_{w2}}{m_{w2}} & 0 \\ 0 & \frac{k_{h3}}{m_e} & -\frac{k_{h3}+k_e}{m_e} & 0 & 0 & -\frac{b_e}{m_e} \end{bmatrix} X \\
&\quad + \begin{bmatrix} 0 & 0 \\ 0 & 0 \\ 0 & 0 \\ \frac{k_{h1}}{m_{w1}} & 0 \\ 0 & 0 \\ 0 & \frac{1}{m_e} \end{bmatrix} \begin{bmatrix} x \\ F_e \end{bmatrix} \\
&= AX + B \begin{bmatrix} x \\ F_e \end{bmatrix}, \\
\begin{bmatrix} F_p \\ x_e \end{bmatrix} &= \begin{bmatrix} -k_{h1} & 0 & 0 & 0 & 0 & 0 \\ 0 & 0 & 1 & 0 & 0 & 0 \end{bmatrix} X + \begin{bmatrix} k_{h1} & 0 \\ 0 & 0 \end{bmatrix} \begin{bmatrix} x \\ F_e \end{bmatrix} \\
&= CX + D \begin{bmatrix} x \\ F_e \end{bmatrix}.
\end{aligned}
\tag{8}
$$

From input to output, the transfer function can be written in a two-port network hybrid matrix [33] form as,

$$
\begin{bmatrix} F_p \\ x_e \end{bmatrix} = C(sI - A)^{-1}B \begin{bmatrix} x \\ F_e \end{bmatrix} = \begin{bmatrix} G_{11} & G_{12} \\ G_{21} & G_{22} \end{bmatrix} \begin{bmatrix} x \\ F_e \end{bmatrix}, \tag{9}
$$

where $G_{21} = -G_{12}$.

B. System Identification

A torque chirp signal (0.001 Hz to 1000 Hz) is put on motor and the generated motor position is considered as one input of system. Even though there's no contact force applied, any friction on end-effector would be the same as contact force for the system. By cancelling the external force input for two output in Eq. 9, the difference between end-effector position and motor position can be represented as:

$$
\begin{aligned}
x_e - x &= -(G_{12}^{-1}G_{11}G_{22} - G_{21} + 1)x + G_{12}^{-1}G_{22}F_p \\
&= H_1 x + H_2 F_p.
\end{aligned}
\tag{10}
$$

Eq. 10 will be used to identify internal hose model by weighted least square with weight tuned focusing on target frequency range. The reason to use $x_e - x$ instead of x_e is that it's easy to see the internal modes excited by high frequency input in Fig. 6b. We choose to focus on below 150 Hz, which is enough for human interaction. This range captures two position difference peak and inspires us to use a 2-DOF model for internal hose. The mean square error of $x_e - x$ in Fig. 6a will converge at 3-DOF model including end-effector.

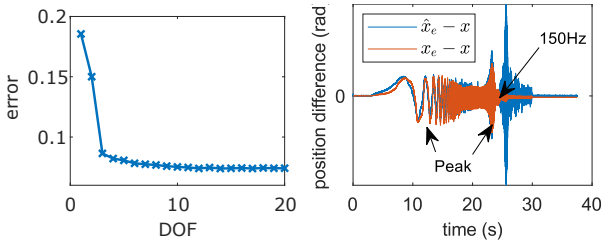

(a) MSE convergence for 0 to 150Hz range (b) $\hat{x}_e - x$ and $x_e - x$ difference

Fig. 6: Model order convergence and estimated $\hat{x}_e - x$

From Eqn 9, the external force can be estimated as:

$$
F_e = G_{12}^{-1}F_p - G_{12}^{-1}G_{11}x. \tag{11}
$$

If friction is ignored on end-effector for free motion, we can directly estimate G_{21} from $\hat{x}_e = G_{21}x$. Notice, only G_{21} is under a frictionless system assumption, H_1 and H_2 should be accurate no matter friction exists or not.

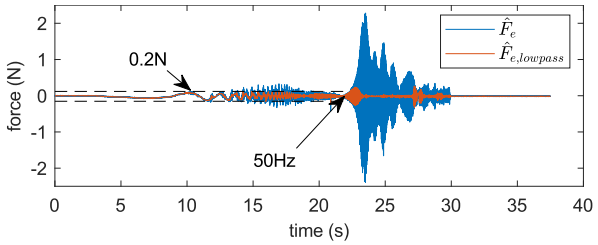

Fig. 7: Estimated external fingertip force

Combine H_1, H_2 and G_{21} together, the external force can be estimated using F_p and x as following:

$$
\begin{aligned}
\hat{F}_e &= G_{12}^{-1}F_p - G_{12}^{-1}G_{11}x \\
&= -G_{21}^{-1}F_p + H_2^{-1}(1 - G_{21}^{-1}H_1 - G_{21}^{-1})x.
\end{aligned}
\tag{12}
$$

A 50 Hz lowpass filter is applied to remove high frequency estimated force error. In ideal case, the estimated force should be zero all the time, but due to model uncertainty (mostly from G_{21}) we would have at most 0.2 N fingertip force error below 50 Hz (filtered data in Fig 7).

C. Force Estimation Test

In this part, we set up a impulse hammer to measure contact force and compare it to the estimated contact force. Due to the applied 50 Hz lowpass filter, the estimated force has a 0.08s lag compared to measured input force. Notice in Fig. 8, the measured force will not go to zero when lose contact. This is because of the property of impulse hammer. It's equivalent to have a built-in highpass filter, and the resulting force will have a reverse peak when suddenly lose contact. On the other hand, the estimated force will go to a small value when lose contact. At the same time, estimated force has 10 times less noise level.

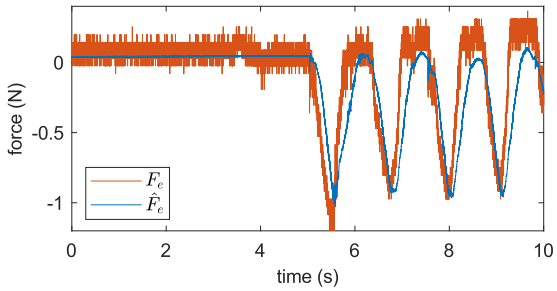

Fig. 8: Measured contact force and estimated contact force

D. Low-noise Force Estimation Approach

In DC or low frequency (below 5 Hz), internal force F_p and virtual spring force $F_a = K_p x$ on motor (red and yellow curve in Fig. 9a) can both be used to roughly estimate of external force since spring behavior dominates at low frequency range. Notice, there's a gap in Fig. 9a between estimated force and equivalent force from pressure when end-effector is away from origin point which is from the stiffness k_e on end-effector coming from diaphragm. Also, we can see $F_a = K_p x$ is closed to F_p. Look closely to data, virtual spring force on motor is slightly behind estimation force from pressure (around 0.01s behind), because force related to motor acceleration and velocity is not included, but it's far less noisy (around 50 times lower) in Fig. 9b.

This result inspires us to set a small virtual spring stiffness (K_p gain in PD controller in Fig. 3) and use $F_a = K_p x$ instead of F_p in Eq. 12. The result is shown in Fig. 10a and Fig. 10b, where low frequency human input is well captured with reduced noise level, which makes it easy to decide a contact happens or not. However, high frequency impulse input is attenuated.

Both original external force estimation using internal force F_p from internal pressure and low-noise approach using virtual spring force $F_a = K_p x$ are useful for different contact type. Original works better for a hard and rigid object contact where contact impulse is at least 10 times than estimated

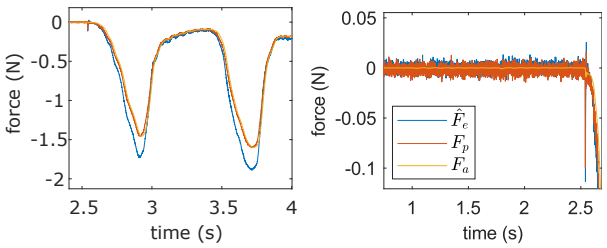

(a) Low frequency interaction (b) Noise comparison

Fig. 9: Comparison between estimated external force $\hat{F}_e$, F_p and $F_a = K_p x$

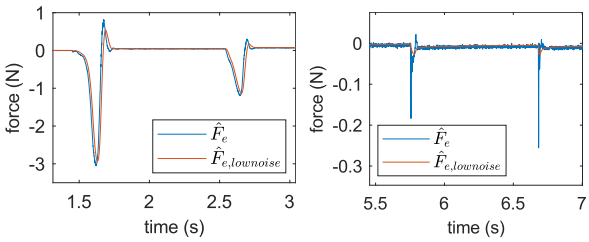

(a) Low frequency input (b) High frequency input

Fig. 10: Original estimated external force and low-noise approach

force noise level. Low-noise approach is better for a slow contact with soft and compliant object where input is in low frequency range. Since both approaches are not in closed-loop feedback system, we can turn them on at the same time and set different threshold for different type of contact. In the supplement video, part (v) shows a rigid object contact using wooden block and (vi) shows a compliant object contact with a seagull feather.

V. CONCLUSIONS

Detecting endpoint contact without external force sensing is challenging under the requirement of maximizing endpoint dynamic impedance range. Discontinuous (Coulomb) friction and deadband (backlash) at motor plant, even when they are unknown, can be eliminated when both motor states and internal force between motor and end-effector is known. But friction and deadband at the endpoint, being entirely unobservable from internal force, must be minimized to the greatest extent possible through actuator topology and material design; hysteresis and viscous friction should be minimized. Estimation of the endpoint state in fluid-actuated systems without explicit endpoint sensing works well using a multi-DOF lumped mass-spring model if endpoint friction is minimized, but model order varies for different physical hardware and different input frequency.

One possible extension for this work is to add an on-line observer to estimate/identify the environment/interaction impedance continuously. This ability would be useful for measuring the stiffness and damping properties of grasped objects, and useful for adaptively tuning manipulator impedance on-the-fly to the optimal value, given the continuously varying environmental impedance.

REFERENCES

[1] C. Lenz and S. Behnke, "Bimanual telemanipulation with force and haptic feedback through an anthropomorphic avatar system," *Robotics and Autonomous Systems*, vol. 161, p. 104338, 2023.

[2] R. Luo, C. Wang, E. Schwarm, C. Keil, E. Mendoza, P. Kaveti, S. Alt, H. Singh, T. Padir, and J. P. Whitney, "Towards robot avatars: Systems and methods for teleinteraction at avatar xprize semi-finals," in *2022 IEEE/RSJ International Conference on Intelligent Robots and Systems (IROS)*, 2022, pp. 7726–7733.

[3] R. v. Ham, T. Sugar, B. Vanderborght, K. Hollander, and D. Lefeber, "Compliant actuator designs," *IEEE Robotics & Automation Magazine*, vol. 3, no. 16, pp. 81–94, 2009.

[4] J. Colgate, M. Stanley, and J. Brown, "Issues in the haptic display of tool use," in *Proceedings 1995 IEEE/RSJ International Conference on Intelligent Robots and Systems. Human Robot Interaction and Cooperative Robots*, vol. 3. Pittsburgh, PA, USA: IEEE Comput. Soc. Press, 1995, pp. 140–145.

[5] W. T. Townsend and J. A. Guertin, "Teleoperator slave-wam design methodology," *Industrial Robot: An International Journal*, vol. 26, no. 3, pp. 167–177, 1999.

[6] D. Whitney, "Historical perspective and state of the art in robot force control," in *Proceedings. 1985 IEEE International Conference on Robotics and Automation*, vol. 2. St. Louis, MO, USA: Institute of Electrical and Electronics Engineers, 1985, pp. 262–268.

[7] S. Eppinger and W. Seering, "Introduction to dynamic models for robot force control," *IEEE Control Systems Magazine*, vol. 7, no. 2, pp. 48–52, 1987.

[8] Chae An and J. Hollerbach, "Dynamic stability issues in force control of manipulators," in *Proceedings. 1987 IEEE International Conference on Robotics and Automation*, vol. 4. Raleigh, NC, USA: Institute of Electrical and Electronics Engineers, 1987, pp. 890–896.

[9] G. Pratt and M. Williamson, "Series elastic actuators," in *Proceedings of the IEEE/RSJ International Conference on Intelligent Robots and Systems*, vol. 1, July 1995, pp. 399 – 406.

[10] J. W. Hurst, J. E. Chestnutt, and A. A. Rizzi, "The actuator with mechanically adjustable series compliance," *IEEE Transactions on Robotics*, vol. 26, no. 4, pp. 597–606, 2010.

[11] C. Majidi, "Soft robotics: a perspective—current trends and prospects for the future," *Soft Robotics*, vol. 1, no. 1, pp. 5–11, 2014.

[12] I. W. Hunter, J. M. Hollerbach, and J. Ballantyne, "A comparative analysis of actuator technologies for robotics," *Robotics Review*, vol. 2, pp. 299–342, 1992.

[13] M. V. Sivaselvan, A. M. Reinhorn, X. Shao, and S. Weinreber, "Dynamic force control with hydraulic actuators using added compliance and displacement compensation," *Earthquake Engineering & Structural Dynamics*, vol. 37, no. 15, pp. 1785–1800, 2008.

[14] A. de Luca and R. Mattone, "Sensorless robot collision detection and hybrid force/motion control," in *Proceedings of the 2005 IEEE International Conference on Robotics and Automation*, 2005, pp. 999–1004.

[15] J. Lee, C. Lee, N. Tsagarakis, and S. Oh, "Residual-based external torque estimation in series elastic actuators over a wide stiffness range: Frequency domain approach," *IEEE Robotics and Automation Letters*, vol. 3, no. 3, pp. 1442–1449, 2018.

[16] Dragan Pršić, Novak Nedić, and Ljubiša Dubonjić, "Modeling and Simulation of Hydraulic Long Transmission Line by Bond Graph," *Journal of Mechanics Engineering and Automation*, vol. 3, no. 4, Apr. 2013.

[17] N. Hogan, "Impedance control: an approach to manipulation. i. theory." *Transactions of the ASME. Journal of Dynamic Systems, Measurement and Control*, vol. 107, no. 1, pp. 1–7, 1985.

[18] B. Vanderborght, A. Albu-Schäffer, A. Bicchi, E. Burdet, D. G. Caldwell, R. Carloni, M. Catalano, O. Eiberger, W. Friedl, G. Ganesh *et al.*, "Variable impedance actuators: A review," *Robotics and autonomous systems*, vol. 61, no. 12, pp. 1601–1614, 2013.

[19] J. W. Sensinger and R. F. F. Weir, "Improvements to series elastic actuators," in *2006 2nd IEEE/ASME International Conference on Mechatronics and Embedded Systems and Applications*. IEEE, 2006, pp. 1–7.

[20] N. Paine, S. Oh, and L. Sentis, "Design and control considerations for high-performance series elastic actuators," *IEEE/ASME Transactions on Mechatronics*, vol. 19, no. 3, pp. 1080–1091, 2013.

[21] N. Hogan and S. Buerger, "Impedance and Interaction Control," in *Robotics and Automation Handbook*, T. Kurfess, Ed. CRC Press, Oct. 2004.

[22] E. Colgate and N. Hogan, "An analysis of contact instability in terms of passive physical equivalents," in *Proceedings, 1989 International Conference on Robotics and Automation*. Scottsdale, AZ, USA: IEEE Comput. Soc. Press, 1989, pp. 404–409.

[23] S. P. Buerger and N. Hogan, "Complementary stability and loop shaping for improved human–robot interaction," *IEEE Transactions on Robotics*, vol. 23, no. 2, pp. 232–244, 2007.

[24] W. S. Newman and Y. Zhang, "Stable interaction control and coulomb friction compensation using natural admittance control," *Journal of Robotic Systems*, vol. 11, no. 1, pp. 3–11, 1994.

[25] J. S. Hart and G. Niemeyer, "Absolutely stable model-based 2-port force controller for telerobotic applications," *The International Journal of Robotics Research*, vol. 33, no. 6, pp. 847–865, 2014.

[26] M. Nakao, K. Ohnishi, and K. Miyachi, "A robust decentralized joint control based on interference estimation," in *Proceedings. 1987 IEEE International Conference on Robotics and Automation*, vol. 4. IEEE, 1987, pp. 326–331.

[27] E. Schwarm, K. M. Gravesmill, and J. P. Whitney, "A Floating-Piston Hydrostatic Linear Actuator and Remote-Direct-Drive 2-DOF Gripper," in *2019 International Conference on Robotics and Automation (ICRA)*. Montreal, QC, Canada: IEEE, May 2019, pp. 7562–7568.

[28] J. P. Whitney, T. Chen, J. Mars, and J. K. Hodgins, "A hybrid hydrostatic transmission and human-safe haptic telepresence robot," in *2016 IEEE International Conference on Robotics and Automation (ICRA)*. IEEE, 2016, pp. 690–695.

[29] H. Shim, G. Park, Y. Joo, J. Back, and N. H. Jo, "Yet Another Tutorial of Disturbance Observer: Robust Stabilization and Recovery of Nominal Performance," *Control Theory and Technology*, vol. 14, no. 3, pp. 237–249, Aug. 2016.

[30] E. R. Kandel, J. H. Schwartz, T. M. Jessell, S. Siegelbaum, A. J. Hudspeth, S. Mack *et al.*, *Principles of neural science*. McGraw-hill New York, 2000, vol. 4.

[31] M. H. Raibert, J. J. Craig *et al.*, "Hybrid position/force control of manipulators," *Journal of Dynamic Systems, Measurement, and Control*, vol. 103, no. 2, pp. 126–133, 1981.

[32] J. E. Colgate, "The Control of Dynamically Interacting System," PhD Thesis, M.I.T. Department of Mechanical Engineering, Aug. 1988.

[33] B. Hannaford, "A design framework for teleoperators with kinesthetic feedback," *IEEE Transactions on Robotics and Automation*, vol. 5, no. 4, pp. 426–434, 1989.